

Numerical validation and influence of optical distortions on accuracy

Clément Ernould^{a,b}, Benoît Beausir^{a,b,*}, Jean-Jacques Fundenberger^{a,b}, Vincent Taupin^{a,b}, and Emmanuel Bouzy^{a,b}

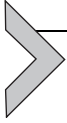
^aUniversité de Lorraine, CNRS, LEM3, Metz, France

^bLaboratory of Excellence on Design of Alloy Metals for low-mAss Structures (DAMAS), University of Lorraine, Metz, France

*Corresponding author: e-mail address: benoit.beausir@univ-lorraine.fr

Contents

1. Introduction	2
1.1 Context	2
1.2 Content of the chapter	3
1.3 Reminder of notations and formula	4
2. Generation of the test datasets	5
2.1 Patterns generated by warping a dynamically simulated master pattern	5
2.2 Motivations	9
2.3 Investigated cases	10
3. Numerical validation and convergence speed	14
3.1 Numerical validation	14
3.2 Initial guess and convergence speed	17
3.3 Variability of the results	22
4. Necessity of a correction of optical distortions	24
4.1 Error in the absence of a correction	24
4.2 Relative error on rotation and elastic strain components	28
4.3 Required accuracy of the distortion model parameters	30
5. Discussion	32
6. Summary	36
6.1 Numerical validation of the method	36
6.2 Influence of optical distortion on accuracy	36
References	37



1. Introduction

1.1 Context

For reminder, the present work was conducted as part of the first author's PhD thesis at the University of Lorraine from 2017 to 2020 (Ernould, 2020). It deals with the development of a high-angular resolution method for the measurement lattice rotations and elastic strains in the scanning electron microscope (Ernould, Beausir, Fundenberger, Taupin, & Bouzy, 2020a, 2020b, 2021). This kind of technique is known as the HR-EBSD or, more recently, the HR-TKD technique, depending on whether it is applied to electron backscatter diffraction (EBSD) patterns or transmission Kikuchi diffraction (TKD) patterns. In the following, "HR-EBSD/TKD" will be employed when no distinction is needed regarding the SEM-based configuration used.

Lattice rotations and elastic strains are deduced from the displacement field between two Kikuchi patterns belonging to the same crystal, as detailed in Chapter "Measuring elastic strains and orientation gradients by scanning electron microscopy: Conventional and emerging methods" by Ernould et al. In pioneering works by (Wilkinson, Meaden, & Dingley, 2006a; Wilkinson, Meaden, & Dingley, 2006b), the displacement field is determined from local translation measurements from small square subsets and an overdetermined and weighted system of equations is then iteratively solved (Britton & Wilkinson, 2011). More recently, global approaches, i.e., considering a unique and large subset, were developed (Ruggles, Bomarito, Qiu, & Hochhalter, 2018; Shi, Roux, Latourte, & Hild, 2019; Vermeij & Hoefnagels, 2018).

The present approach belongs to this second type. Chapter "Development of a homography-based global DIC approach for high-angular resolution in the SEM" by Ernould et al. demonstrated the displacement field in the scintillator sought by the HR-EBSD/TKD technique is mathematically equivalent to a linear homography. Knowing the SEM projection geometry and its variations across the orientation map, lattice rotations and elastic strains can be deduced from the homography. Its measurement is relying on established digital image correlation (DIC) techniques in the field of experimental mechanics, which were here transferred to electron diffraction patterns. More specifically, patterns are pre-aligned by means of global image cross-correlation techniques and the eight deformation parameters of the homography are then measured with subpixel accuracy by means of an inverse-compositional Gauss-Newton (IC-GN) algorithm.

The implementation of the method is extensively described in Chapter “[Implementing the homography-based global HR-EBSD/TKD approach](#)” by Ernould et al., in particular the working principle of a correction of optical distortions integrated in the IC-GN algorithm. It enables the homography to be measured directly from optically distorted patterns, reducing the numerical cost of the whole analysis. Considering the current state of the code, the extra cost of the correction appeared negligible as compared to the pattern pre-processing step conducted until present to remove the effects of optical distortions. This is related to the runtime required to compute the interpolation coefficients of the original (distorted) image. The question now is whether the proposed correction is truly effective and under what circumstances it is necessary. More generally, the correct implementation of the method must be verified and some aspects like the convergence criterion of the IC-GN algorithm also need to be clarified.

1.2 Content of the chapter

This chapter proposes a numerical validation of the homography-based global HR-EBSD/TKD approach. Angular disorientation in the range 0 to 14° as well as equivalent elastic strains up to 5×10^{-2} are considered. They cover the conditions with which the technique is usually confronted in practice. Beyond the validation of the method itself, aim is also to quantify the effects of optical distortion.

First, test conditions are presented. Test images are not the result of individual simulations but generated by interpolating a dynamically simulated electron diffraction pattern. This procedure allows many cases to be investigated, but there are other motivations that will be discussed.

In a second step, the homography-based global approach is validated in the absence of optical distortions, and then using the correction when the images are subjected to first-order radial distortion. The performance of the global cross-correlation based pattern pre-alignment technique is evaluated in terms of angular accuracy as well as its consequences regarding the convergence speed of the IC-GN algorithm. The influence of the convergence criterion or of a median or Gaussian spatial filter is also studied.

In a third step, the error induced by neglecting a first-order radial distortion is quantified, demonstrating the necessity of a correction. This calls into question some common ideas in the literature of the HR-EBSD/TKD technique. Finally, the accuracy on the parameters of the distortion model to ensure the effectiveness of the correction is evaluated.

1.3 Reminder of notations and formula

Let $(\overrightarrow{X_1}, \overrightarrow{X_2}, \overrightarrow{X_3})$ be the scintillator's frame, whose axes $\overrightarrow{X_1}$ and $\overrightarrow{X_2}$ are aligned with the scintillator's horizontal and vertical edges, respectively. $\overrightarrow{X_1}$ is rightwards and $\overrightarrow{X_2}$ is downwards to be consistent with the usual matrix representation of images. For the sake of clarity, points belonging to the scintillator are denoted in two ways:

- Uppercase letters, $\mathbf{X} = [X_1 \ X_2]^T$, mean that absolute (or pixel) coordinates are considered. The origin is the upper left corner of the scintillator.
- Lowercase letters, $\mathbf{x} = [x_1 \ x_2]^T$, mean that relative coordinates with respect to pattern center (*PC*) are considered. The latter admits $\mathbf{X}^{PC} = [X_1^{PC} \ X_2^{PC}]^T$ as absolute coordinates, i.e., $x_i = X_i - X_i^{PC}$ ($i=1, 2$).

By default, coordinates in the optically undistorted configuration are considered since it is the one in which the linear homography assumption is valid. The transition from the undistorted configuration (taking place in the scintillator) and the distorted one (recorded by the camera sensor) is described by the distortion model D , which depends on each camera:

$$\tilde{\mathbf{X}} = D(\mathbf{X}), \quad (1)$$

the position in the optically distorted images being highlighted by a tilde. Note that the optical center is invariant by the distortion model, so it is uniquely denoted as $\mathbf{X}_{opt} = [X_1^{opt} \ X_2^{opt}]^T$ in this chapter.

Regarding the linear homography measured by the IC-GN algorithm, its deformation parameters h_{ij} are stored in the deformation vector

$$\mathbf{p} = [h_{11} \ h_{12} \ h_{13} \ h_{21} \ h_{22} \ h_{23} \ h_{31} \ h_{32}]^T, \quad (2)$$

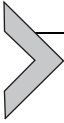
and arranged in the shape function \mathbf{W} as follows (Baker & Matthews, 2004; Hartley & Zisserman, 2004):

$$\mathbf{W}(\mathbf{p}) = \begin{bmatrix} 1 + h_{11} & h_{12} & h_{13} \\ h_{21} & 1 + h_{22} & h_{23} \\ h_{31} & h_{32} & 1 \end{bmatrix}. \quad (3)$$

Similarly, Δh_{ij} denote the parameters of the increment deformation vector $\Delta \mathbf{p}$, which is computed at each iteration of the IC-GN algorithm. The convergence criterion C_{conv} is fulfilled when the norm

$$\|\Delta\mathbf{p}\| = \sqrt{\sum_{i=1}^3 ((\xi_{1\max} \cdot \Delta h_{i1})^2 + (\xi_{2\max} \cdot \Delta h_{i2})^2) + \Delta h_{13}^2 + \Delta h_{23}^2} \quad (4)$$

is lower or equal than a threshold. The latter was set to 0.001 pixel according to the literature (Pan, Li, & Tong, 2013; Shao, Dai, & He, 2015; Zhang et al., 2015) in Chapter “Implementing the homography-based global HR-EBSD/TKD approach” by Ernould et al. In Eq. (4), $\xi_{1\max} = \max |\xi_1^{(i)}|$ and $\xi_{2\max} = \max |\xi_2^{(i)}|$ where $\xi_k^{(i)} = X_k - X_{0k}$ ($k=1,2$) are the coordinates of the i -th point forming the subset ($i \in \llbracket 1, N \rrbracket$) relative to the arbitrary point $\mathbf{X}_0 = [X_{01} \ X_{02}]^T$. In practice, the subset’s geometric center is considered.



2. Generation of the test datasets

This section describes the generation process of the test images as well as the cases studied. As test images are not the result of individual dynamic pattern simulations, motivations for this choice are detailed.

2.1 Patterns generated by warping a dynamically simulated master pattern

2.1.1 Overview of the procedure

A master pattern of unstrained aluminum at 20 keV is dynamically simulated using the compiled version of EMSOFT 4.2 software (Singh, Ram, & Graef, 2017). Table 1 summarizes the simulation parameters. This master pattern accounts for the entire Kikuchi sphere. Actually, it was already displayed in fig. 7 in Chapter “Measuring elastic strains and orientation gradients by scanning electron microscopy: Conventional and emerging methods” by Ernould et al.

A diffraction pattern of arbitrary orientation (75° , 125° , 15°) and of size 2400×2400 -pixels with a pixel size of $20 \mu\text{m}$ is then extracted from the master pattern. It is denoted as “source image” and it is showed in the bottom right of Fig. 1. Test images of size 1200×1200 -pixel with same pixel size are then extracted by interpolating this “source image.” This is outlined by the light-blue line in Fig. 1, while the reference pattern corresponds to the central region delimited by a white dash-line. The pixel size and resolution of the test pattern are chosen according to the maximum resolution of the Bruker e-Flash HR+ camera used during this work.

Regarding the projection geometry, a typical EBSD configuration with a sample-to-detector distance DD of 16 mm is assumed, as schematized in the

Table 1 Parameters of the dynamical pattern simulation in EMsoft 4.2.**Material**

Material	Aluminum
Structure	FCC
Lattice parameter	0.4 nm
Debye-Waller factor	0.004 nm^2

Monte Carlo simulation

Total number of incident electrons	2×10^9
Specimen tilt angle	70°
Incident beam energy	20 keV
Minimum backscatter electron exit energy	15 keV
Energy bin size	1 keV
Maximum exit depth	100 nm
Depth step size	1 nm

Master pattern simulation

Smallest D-spacing	0.05 nm
Master pattern size	1000 (2001 \times 2001)
Bethe parameters	4 / 8 / 50

Pattern simulation parameters

Camera elevation	0°	Energy range (min)	20 keV
Euler angles	(75° , 125° , 15°)	Energy range (max)	20 keV
Detector size	2400×2400	Include background	No
Detector pixel size	$20 \mu\text{m}$	Include Poisson noise	No
Sample-to-detector distance	16 mm	Gamma	0.33
Pattern center location	0, 0 (centered)	Bit depth	16-bit

top of Fig. 1. Red arrows show the steps involved in the computation of a target pattern. Starting from one of its pixels, the antecedent position to interpolate in the source image must be determined. This requires inverting the optical distortion effects as well as those of the transformation F^c and the probe displacement δPC at the sample surface.

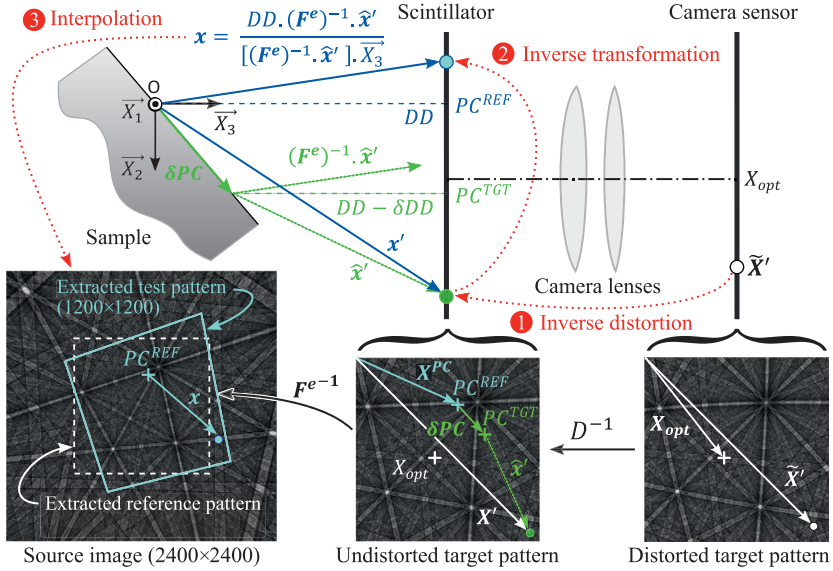


Fig. 1 Sketch of the HR-EBSD geometry. The patterns of size 1200×1200 are constructed by interpolating a simulated pattern of unstrained aluminum of size 2400×2400 (called "source image").

2.1.2 Inverting optical distortions

First, the antecedent X' in the undistorted configuration (i.e., in the scintillator) of a point \tilde{X}' in the distorted configuration (i.e., in the pattern recorded by the camera) is determined from the inverse distortion model D^{-1} . In practice, the user can use potentially complex models D as a correction, and knowing their inverse is not necessary. Inverting optical distortions is commonly accompanied by nonlinearity problems. Therefore, the numerical validation is here limited to a quite simple model, namely first-order radial distortion:

$$D : \begin{pmatrix} \tilde{X}_1 \\ \tilde{X}_2 \end{pmatrix} = \begin{pmatrix} X_1 \\ X_2 \end{pmatrix} + (K_1 \cdot r^2) \cdot \begin{pmatrix} \Delta_1 \\ \Delta_2 \end{pmatrix}, \quad (5)$$

where $\Delta_i = X_i - X_i^{opt}$ ($i = 1, 2$) and $r = \sqrt{\Delta_1^2 + \Delta_2^2}$.

This model is chosen as it admits an exact inverse, which is a 9th order radial distortion (Drap & Lefèvre, 2016):

$$D^{-1} : \begin{pmatrix} X_1 \\ X_2 \end{pmatrix} = \begin{pmatrix} \tilde{X}_1 \\ \tilde{X}_2 \end{pmatrix} + \sum_{i=1}^9 b_i \cdot r^{2i} \cdot \begin{pmatrix} \Delta_1 \\ \Delta_2 \end{pmatrix} \quad (6)$$

where $\Delta_i = \tilde{X}_i - X_i^{opt}$ ($i=1, 2$). The nine distortion coefficients b_i are analytically deduced from K_1 in Eq. (5) as follows:

$$\left\{ \begin{array}{l} b_1 = -K_1 \\ b_2 = 3.K_1^2 \\ b_3 = -12.K_1^3 \\ b_4 = 55.K_1^4 \\ b_5 = -273.K_1^5 \\ b_6 = 1428.K_1^6 \\ b_7 = -7752.K_1^7 \\ b_8 = 43263.K_1^8 \\ b_9 = -246675.K_1^9 \end{array} \right. . \quad (7)$$

Note that formula inverting radial distortion up to the fourth order are given in the reference.

Here, radial distortion is limited to the first-order for two reasons. On the one hand, it has a predominant effect while the third-order or higher terms are generally negligible (Wang, Shi, Zhang, & Liu, 2008). This model is thus commonly used, including by (Britton et al., 2010) and (Mingard, Day, Maurice, & Queded, 2011) as far as the HR-EBSD/TKD technique is concerned. On the other hand, numerical instability issues worsen with increasing distortion order, as pointed out by (Drap & Lefèvre, 2016). In the present study, the inversion of a first-order radial distortion already involves the multiplication of very large numbers ($r^{18} \approx 10^{52}$) with very small ones ($K_1^9 \approx 10^{-63}$).

2.1.3 Inverting the transformation

The position \mathbf{X}' in the scintillator being identified, the second step (red arrow in Fig. 1) is the computation of its antecedent \mathbf{X} in the scintillator by \mathbf{F}^e and the effects of the probe displacement δPC .

Positions relative to the PC must be considered, namely $\mathbf{x}' = \mathbf{X}' - \mathbf{X}^{PC}$ in the target pattern and its matching point $\mathbf{x} = \mathbf{X} - \mathbf{X}^{PC}$ in the reference pattern. For a fixed geometry ($\delta PC = \mathbf{0}$), the antecedent \mathbf{x} is computed from its

image \mathbf{x}' by \mathbf{F}^e as follows (see section 3.1 in Chapter “Measuring elastic strains and orientation gradients by scanning electron microscopy: Conventional and emerging methods” by Ernould et al.):

$$\mathbf{x} = \frac{DD}{(\mathbf{F}^{e-1} \cdot \mathbf{x}') \cdot X_3} \left(\mathbf{F}^{e-1} \cdot \mathbf{x}' \right). \quad (8)$$

Otherwise, \mathbf{x}' must be substituted by $\hat{\mathbf{x}}' = \mathbf{x}' - \delta PC$ in Eq. (8), as shown by green arrows in Fig. 1.

All that remains is to deduce the position to interpolate in the source image. This only requires adding an offset of 600 pixels to the absolute coordinates $\mathbf{X} = \mathbf{x} + \mathbf{X}^{PC}$ as the reference pattern is centered in the source image. In the absence of any specific mention, interpolation is performed using the biquintic B-splines coefficients, like the IC-GN algorithm does during image registration.

2.2 Motivations

The test patterns are not the result of individual simulations, but they are regions extracted from a dynamically simulated pattern. There are several reasons for this choice.

First, this approach allows pattern generation and registration to be performed using the same interpolation scheme. The interpolation bias is then greatly reduced but not completely eliminated (Bornert et al., 2017). On the one hand, the effect of the interpolation bias could be visualized by occasionally generating patterns by bicubic interpolation of the source image. On the other hand, the reduction of the interpolation bias and the absence of possible errors or approximations intrinsic to the simulation make it possible to better isolate optical distortion effects. This second point is particularly important when estimating the required accuracy of the distortion model parameters.

Second, the present approach is supported by previous studies of the accuracy the HR-EBSD/TKD technique. Experimental or dynamically simulated patterns are necessary to prove the validity of the mechanical model describing the expected displacement field on the scintillator. Indeed, the latter does not consider some diffraction phenomena such as the variation of band contrast with orientation or the change in bandwidth under the effect of elastic strains.

The influence of band contrast was legitimately raised by (Maurice, Driver, & Fortunier, 2012), as they proposed the remapping technique.

The authors did not observe an increase in error when applying the local HR-EBSD/TKD approach to dynamically simulated patterns disoriented up to 15° . The same trend was reported by (Vermeij & Hoefnagels, 2018) using a global HR-EBSD/TKD approach. Dynamically simulated patterns involving disorientation up to 12° were considered, as well as equivalent elastic strains of 5×10^{-4} , 2×10^{-3} , and 1×10^{-2} . According to the authors, the variations in bandwidth do not call into question the validity of the mechanical model, even when elastic strains are of the order of 1%. Although they noticed the error worsens with equivalent elastic strain, it was $\sim 2 \times 10^{-5}$ at most, i.e., well below the 1×10^{-4} accuracy commonly attributed to the HR-EBSD/TKD technique under ideal experimental conditions.

More generally, none of the many studies conducted over the past 15 years using experimental patterns (McLean & Osborn, 2018; Plancher, 2015; Plancher et al., 2016; Shi et al., 2019; Villert, Maurice, Wyon, & Fortunier, 2009; Wilkinson et al., 2006a; Yu, Liu, Karamched, Wilkinson, & Hofmann, 2019) or simulated patterns (Britton et al., 2010; Britton & Wilkinson, 2011, 2012; Maurice et al., 2012; Ruggles et al., 2018; Vermeij & Hoefnagels, 2018) have questioned the relevance of the mechanical model (Villert et al., 2009; Wilkinson et al., 2006b).

Since the diffraction effects omitted in the present test images are second order, this chapter proposes a numerical validation of the method by showing that it is able to correctly determine a displacement field described by the mechanical model sought by the HR-EBSD/TKD technique. The test images are nevertheless extracted from a dynamically simulated pattern, so that they are representative of the intended application in terms of intensity distribution and gradients. Moreover, their generation being much less numerically expensive than individual simulations, hundreds of cases can be investigate.

2.3 Investigated cases

Unless otherwise stated, the pattern center of the reference pattern admits is $\mathbf{X}^{PC} = [625400]^T$ and the sample-to-detector distance is 16 mm. This is typical of EBSD patterns. The projection geometry of target patterns differs by $\delta\mathbf{PC} = [5 - 3 - 1.0919]^T$ pixels from that of the reference, corresponding to a probe displacement of about $115 \mu\text{m}$ at the sample's surface associated with an increase in sample-to-detector distance by $21.838 \mu\text{m}$ ($1.0919 \times 20 \mu\text{m}/\text{pixel}$). Indeed, a negative variation along $\overline{X_3}$ pointing toward the scintillator means the probe gets further from it. Note that such a probe displacement is quite

large for HR-EBSD mappings but not unlikely. Aim is, among others, to ensure the IC-GN algorithm correctly captures the isotropic scale of the pattern induced by the variation in sample-to-detector distance, which is ignored by the proposed pattern pre-alignment method.

Elastic strain states representative of small levels in metals ($<2 \times 10^{-3}$) as well as larger ones in semiconductors (of the order of 10^{-2}) are considered, all in the presence of disorientations up to 14° . This value is typical of intra-granular disorientations in plastically deformed polycrystals, whose grains are usually detected from local orientations by setting a tolerance angle of 5 or 15° between adjacent pixels of the map.

In total, a dataset consists in 1416 test conditions, which are divided into two groups. For the first one, the disorientation angle $\Delta\theta$ varies from 0.1 to 14° . As detailed in Table 2, there are 118 cases: 58 for which disorientation is equally distributed on the three axes and 60 cases for which a single axis carries the rotation (20 cases per axis and the applied disorientations are in bold in the table). The sign of each rotation is random. These 118 cases

Table 2 Overview of the test cases with a disorientation angle ranging from 0.1 to 14° . **118 = 58 + 3 × 20 cases with varying disorientation angle $\Delta\theta$**

58 cases	20 cases*			20 cases*			20 cases*							
$w_{1,2,3} = \pm\Delta\theta/\sqrt{3}$	$w_1 = \pm\Delta\theta, w_{2,3} = 0$			$w_2 = \pm\Delta\theta, w_{1,3} = 0$			$w_3 = \pm\Delta\theta, w_{1,2} = 0$							
*Corresponding to values in bold hereafter														
where $\Delta\theta \in [0.1^\circ, 14^\circ]$														
0.10	0.11	0.12	0.13	0.14	0.15	0.16	0.17	0.18	0.19	0.20	0.22	0.24		
0.26	0.28	0.30	0.33	0.37	0.40	0.45	0.50	0.60	0.70	0.80	0.90	1.0	1.1	1.2
1.3	1.4	1.5	1.6	1.7	1.8	1.9	2.0	2.2	2.4	2.6	2.8	3.0	3.3	3.7
4.0	4.5	5.0	6.0	7.0	8.0	9.0	10.0	10.3	10.7	11.0	11.5	12.0	13.0	14.0
6 strain states with varying von Mises equivalent elastic strain ϵ_{vm}														
ϵ_{vm}	Unstrained	$\sim 5 \times 10^{-4}$			$\sim 2 \times 10^{-3}$			$\sim 5 \times 10^{-3}$			$\sim 1 \times 10^{-2}$		$\sim 2 \times 10^{-2}$	
$\epsilon_{11} [10^{-4}]$	0	1.7			−10			−11			50		83	
$\epsilon_{12} [10^{-4}]$	0	−2.3			6			22			−41		96	
$\epsilon_{13} [10^{-4}]$	0	2.5			−11			24			52		77	
$\epsilon_{22} [10^{-4}]$	0	−1.9			5			16			−44		95	
$\epsilon_{23} [10^{-4}]$	0	2			9			25			−30		83	
$\epsilon_{33} [10^{-4}]$	0	0			0			0			0		0	

Table 3 Overview of the test cases with an equivalent elastic strain ranging from 1×10^{-4} to 5×10^{-2} .

118 = 58 + 3 × 20 cases with varying von Mises equivalent elastic strain ϵ_{vm}														
60 cases	12 cases*		12 cases*		12 cases*		12 cases*		12 cases*		12 cases*			
$\epsilon_{ij} = \pm \sqrt{(3 \cdot \epsilon_{vm}^2)/16}$	$\epsilon_{11} = \epsilon_{vm}$	$\epsilon_{12} = \epsilon_{vm}$	$\epsilon_{13} = \epsilon_{vm}$	$\epsilon_{22} = \epsilon_{vm}$	$\epsilon_{23} = \epsilon_{vm}$									
except $\epsilon_{33} = 0$	$\epsilon_{ij} = 0$ for all other strain components													
* Corresponding to values in bold hereafter														
where $\epsilon_{vm} \in [1 \times 10^{-4}, 5 \times 10^{-2}]$														
$\times 10^{-4}$	1	2	3	4	5	6	7	8	9	10	12	14	16	
18	20	22	24	26	28	30	32	34	36	38	40	42	44	46
48	50	52.5	55	57.5	60	62.5	65	67.5	70	72.5	75	77.5	80	82.5
85	87.5	90	95	100	125	150	175	200	250	300	350	400	450	500
6 disorientation angles $\Delta\theta$														
$\Delta\theta [^\circ]$	0	~0.3	~0.6	~1	~1.5	~3								
$w_1 [^\circ]$	0	0.173	0.346	0.577	0.866	1.732								
$w_2 [^\circ]$	0	0.173	0.346	0.577	0.866	1.732								
$w_3 [^\circ]$	0	0.173	0.346	0.577	0.866	1.732								

are then combined with six complex elastic strain states corresponding to an equivalent von Mises elastic strain ϵ_{vm} of 0 (unstrained), 5×10^{-4} , 2×10^{-3} , 5×10^{-3} , 1×10^{-2} and 2×10^{-2} .

The second group of test conditions, summed up in Table 3, is constructed similarly to the first one. This time, the equivalent elastic strain ϵ_{vm} varies between 1×10^{-4} and 5×10^{-2} considering 118 cases: 58 for which elastic strain components are equal in absolute value (except $\epsilon_{33} = 0$) and 60 cases for which the deformation is applied through a single component (12 cases per component, expect ϵ_{33} , whose value is in bold in the table). Again, the sign of each component is random. These 118 cases are combined with six disorientation angles $\Delta\theta$, namely 0° , 0.3° , 0.6° , 1° , 1.5° , and 3° . Small disorientations are preferred because elastic strains are usually measured in purely elastically deformed or slightly plastically deformed metals.

Note that ϵ_{33} is systematically zero. This is because the HR-EBSD/TKD technique is insensitive to hydrostatic dilatation. Only the deviatoric deformation gradient is $\hat{\mathbf{F}}^e$ is determined from the observed displacement field on the scintillator. This uncertainty is commonly removed by assuming a

traction-free surface, as explained in Chapter “Measuring elastic strains and orientation gradients by scanning electron microscopy: Conventional and emerging methods” by Ernould et al. (section 3.1.3). However, this requires expressing the results in the sample frame. Not to introduce unnecessary calculations with respect to the purpose of this study, all elastic strain and rotation components are here expressed in the scintillator’s frame and ε_{33} is zero so that $\widehat{\mathbf{F}}^e$ equals \mathbf{F}^e . In this way, elastic strain and rotation components in input can be directly face to those derived from the DIC measurements in the scintillator’s frame.

The elastic deformation gradient tensor \mathbf{F}^e is computed considering a “finite rotations – small strains” framework (see section 3.1.4 in Chapter “Measuring elastic strains and orientation gradients by scanning electron microscopy: Conventional and emerging methods” by Ernould et al. for more details):

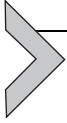
$$\mathbf{F}^e = \begin{bmatrix} 1 + \varepsilon_{11} & \varepsilon_{12} & \varepsilon_{13} \\ \varepsilon_{12} & 1 + \varepsilon_{22} & \varepsilon_{23} \\ \varepsilon_{13} & \varepsilon_{23} & 1 + \varepsilon_{33} \end{bmatrix} \begin{bmatrix} c_2 \cdot c_3 & s_1 \cdot s_2 \cdot c_3 - c_1 \cdot s_3 & c_1 \cdot s_2 \cdot c_3 + s_1 \cdot s_3 \\ c_2 \cdot s_3 & s_1 \cdot s_2 \cdot s_3 + c_1 \cdot c_3 & c_1 \cdot s_2 \cdot s_3 - s_1 \cdot c_3 \\ -s_2 & s_1 \cdot c_2 & c_1 \cdot c_2 \end{bmatrix} \quad (9)$$

where $c_i = \cos(w_i)$, $s_i = \sin(w_i)$ and w_i the rotation with respect to $\overrightarrow{X_i}$, i.e.,

$$\begin{cases} w_1 = w_{32} \\ w_2 = w_{13} \\ w_3 = w_{23} \end{cases} \quad (10)$$

This tensor describes the transition from the crystal state associated with the reference pattern to the one associated with the target pattern.

(Mingard et al., 2011) measured the first-order radial distortion coefficient, i.e., K_1 in Eq. (5), of several EBSD cameras as well as the position of their optical center. Among those having a resolution of about 1000×1000 pixels, barrel distortion ($K_1 < 0$) close to -3×10^{-8} was observed in average. The extreme values were -7×10^{-8} and 3×10^{-8} . Regarding the optical center, it was most often between ~ 15 to ~ 55 pixels away from the center of the screen. Consequently, and unless otherwise stated, the patterns are generated by placing the optical center at $\mathbf{X}_{opt} = [570 \ 620]^T$, i.e., ~ 36 pixels from the image center. Eleven values of K_1 are considered: 0 (distortion-free), 3, 1, -0.5 , -1 , -2 , -3 , -4 , -5 , -7 or -9 ($\times 10^{-8}$). There are therefore as many datasets of 1416 cases each.



3. Numerical validation and convergence speed

This section first numerically validates the homography-based approach and its integrated correction of optical distortions. It also highlights the influence of interpolation bias on accuracy, allowing a better understanding of the motivations detailed in [Section 2.2](#). Then, it assesses the angular accuracy of the global cross-correlation based initial guess. The latter is discussed in the light of the convergence speed of the IC-GN algorithm. To this end, both partial or complete initializations of the homography are considered (see Chapter “Implementing the homography-based global HR-EBSD/TKD approach” by Ernould et al., section 4.2.4), as well as an “ideal” initial guess with perfectly a priori known rotations. Finally, the influence of the convergence criterion C_{conv} or of a median or Gaussian spatial filter on accuracy and convergence speed is studied.

3.1 Numerical validation

3.1.1 Parameters of the DIC analysis and definition of the error

Unless otherwise stated, no filter is applied to the images, since no continuous background is present ([Table 1](#)). The point X_0 coincides with the geometric center of the images. It is also the center of the subsets of size 1024×1024 pixels for the global cross-correlation initial guess and 901×901 pixels for the IC-GN algorithm. The complete initialization of the homography is considered. Biquintic B-splines coefficients are used for interpolation and the convergence criterion is set to 0.001 pixels. Rotations and elastic strains are determined from the left polar decomposition of \mathbf{F}^e (Eq. (9)), which is also considered for pattern generation.

The error is calculated for each rotation or elastic strain component by taking the absolute value of the difference between the measured and the input values. Subsequently, the maximum error.

$$E = \max \left(\left| \varepsilon_{ij} - \varepsilon_{ij}^{input} \right|, \left| \omega_{ij} - \omega_{ij}^{input} \right| \right), \quad (11)$$

or the maximum relative error (in percent)

$$E_r = 100 * \max \left(\left| \frac{\varepsilon_{ij} - \varepsilon_{ij}^{input}}{\varepsilon_{ij}^{input}} \right|, \left| \frac{\omega_i - \omega_i^{input}}{\omega_i^{input}} \right| \right), \quad (12)$$

where $i, j \in \llbracket 1, 3 \rrbracket$ are considered. Note that zero components in input are ignored in the calculation of E_r .

3.1.2 Validation of the approach

Optically undistorted patterns are first considered (no correction needed). The maximum errors as a function of disorientation angle (Fig. 2A) and as a function of equivalent elastic strain (Fig. 2B) are shown as gray regions bounded by the minimum and maximum of the maximum error among the six elastic strain states (Table 2) or disorientation angles (Table 3) studied, respectively. Indeed, no significant difference is observed between them.

The error is relatively constant and is typically 5×10^{-7} . Of course, such a low value stems from the nature of the images used. The strong reduction of the interpolation bias (Section 2.2) is another determining factor, as will be highlighted later. However, an increase in the error is observed at the largest disorientations with a maximum of about 1×10^{-5} . It is mainly attributed to the introduction of noise as the warped target subset goes out of the image.

Optically distorted patterns with K_1 values ranging from -9×10^{-8} to 3×10^{-8} are now analyzed, the exact optical center coordinates and distortion coefficient being prescribed for the integrated correction. The maximum error is again represented by gray regions, as a function of the disorientation angle (Fig. 2C) and as a function of the equivalent elastic strain (Fig. 2D). In the first case, the gray region is delineated from the minimum and maximum of the observed error among all six deformation states and for the ten K_1 values studied. In the second case, the approach is similar except that the cases without rotation ($\Delta\theta = 0^\circ$) are treated separately. These indeed show higher errors at low equivalent elastic strain, the maximum of which is represented by a black dashed line in Fig. 2D.

Overall, the maximum error is typically 5×10^{-6} , which is about an order of magnitude higher than in the absence of optical distortion (black region in Fig. 2A,B). In addition, the error dispersion is also much wider, namely about $\sim 1 \times 10^{-5}$. However, the error levels are too low to conclude that the correction introduces a noticeable error. The principle of the integrated optical distortion correction is thus validated. Rather, these differences illustrate the numerical instability concerns mentioned earlier regarding the inversion of the distortion model. Anyway, their importance is marginal as compared to other factors like interpolation bias, as discussed now.

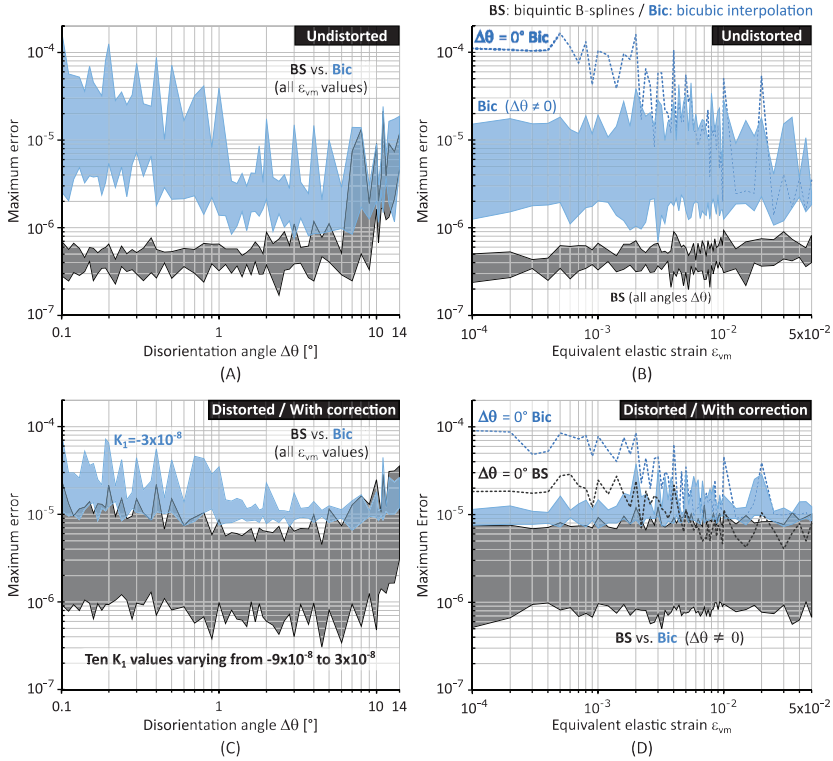


Fig. 2 Maximum error when the test patterns are extracted from the source image using biquintic B-splines coefficients (black) or bicubic interpolation (blue). (A, B) Error in the absence of optical distortion. (C, D) Error when using the integrated correction in the presence of first-order radial distortion. Error (A, C) as a function of the disorientation angle $\Delta\theta$ and (B, D) as a function of the equivalent elastic strain ϵ_{vm} .

3.1.3 Influence of the interpolation bias on accuracy

In order to illustrate the influence of interpolation bias on accuracy, test images are now generated by bicubic interpolation of the source image. A first dataset containing distortion-free patterns is constructed and a second one is subject to a typical radial distortion of $K_1 = -3 \times 10^{-8}$.

The error is represented just like before, but in blue regions in Fig. 2. It is higher than when the same interpolation scheme is used for pattern generation and registration (gray regions), as expected according to (Bornert et al., 2017). However, the maximum error remains almost always below 1×10^{-4} so validity of the proposed method is still not called into question. Interpolation bias overwhelms the previously observed differences in error between using the distortion-free patterns and those analyzed using the

correction. The influence of the correction is only visible through the lower limit of the blue regions. As already observed in the case of biquintic B-splines, it is higher with correction (close to 1×10^{-5} in Fig. 2C,D) than without (1×10^{-6} in Fig. 2A,B), which is still attributed to numerical instabilities.

Surprisingly, the optical distortion-free dataset leads to the highest error, but the difference with respect to distorted patterns remains marginal. In both cases, the error is closed to 1×10^{-4} at the lowest disorientations in the range $0.1\text{--}0.2^\circ$ in Fig. 2A,C, as well as at equivalent elastic strain below $\sim 2 \times 10^{-3}$ in the absence of rotation in Fig. 2B,D (blue dash-line). Interestingly, the error gradually decreases as the equivalent elastic strain increases and merges with the level of error associated with the other five disorientation angles when $\epsilon_{vm} \geq \sim 5 \times 10^{-3}$, i.e., when the effects of elastic strains are as large as those of rotations ($0.3^\circ \approx 5 \times 10^{-3}$ rad).

3.2 Initial guess and convergence speed

Performances of the global cross-correlation based pattern pre-alignment method is evaluated from undistorted patterns having the same projection geometry ($\delta PC = 0$). Its angular error is first measured and discussed. Then the partial ($h_{31} = h_{32} = 0$) and complete homography initializations are compared in terms of convergence speed of the IC-GN algorithm. The results are also discussed in the light of an “ideal” estimate of the solution, i.e., the rotations are a priori known exactly.

3.2.1 Rotation assessment from the global cross-correlation based initial guess

The angular error of the initial guess is defined as the disorientation angle between the estimated and the true solution. This angle is zero in the case of an “ideal” initial guess, so only the contribution of elastic strains remains to be determined.

As detailed in section 4.2 in Chapter “Implementing the homography-based global HR-EBSD/TKD approach” by Ernould et al., the global cross-correlation based pattern pre-alignment relies on an in-plane rotation and a translation measurement, from which relative rotations of the crystal are estimated. They are identical depending on whether the homography is initialized partially (six parameters) or completely (eight parameters). Indeed, the initialization only affects the shape of the initially warped target subset (a square or a uncross quadrilateral, respectively).

Fig. 3A,B shows the angular error of the initial guess when the applied disorientation or equivalent elastic strain are equally distributed among all components, respectively. Extreme cases for which a single component is non-zero are omitted at this point. The initial guess is typically disoriented by 0.25° or less from the solution as long as $\varepsilon_{vm} \leq 5 \times 10^{-3}$ and $\Delta\theta \leq 2^\circ$, and by $0.5^\circ \pm 0.25^\circ$ otherwise. The presence of large disorientations appears at first sight less problematic than the one of equivalent elastic strain of the order of 1% or more. Indeed, the angular accuracy of the initial guess degrades sharply in Fig. 3B while a gap is observed between the brown curve ($\varepsilon_{vm} = 2 \times 10^{-2}$) and the other ones in Fig. 3A.

3.2.2 Influence of gnomonic distortion

Fig. 3c shows the angular error when the total disorientation is carried by a single rotation component. Only the case $\varepsilon_{vm} = 5 \times 10^{-3}$ is displayed for illustrative purposes and the orange curve in Fig. 3A is reported in black to ease comparison. The error is the highest regarding the rotation w_{13} (blue line), which is mainly responsible for a horizontal translation of the patterns see fig. 7 in Chapter “Implementing the homography-based global HR-EBSD/TKD approach” by Ernould et al.). Since the PC is placed 33% of the pattern half-width above the image center, the top of the patterns is less distorted by the gnomonic projection than their bottom. Conversely, the left and right sides are almost equally affected by gnomonic distortion since the PC is 4% of the pattern half-width away from the center along the horizontal direction. Consequently, the error remains quasi constant regarding the rotation w_{32} (green line), which primarily shifts of the pattern vertically. Asymmetry of the gnomonic projection effects at the pattern scale thus appears more harmful for rotation assessment than gnomonic distortion itself.

The error is also relatively constant over the investigated disorientation range regarding the rotation w_{21} (red line), which induces an in-plane rotation of the pattern with respect to the PC. Radial effects of the gnomonic distortion are also centered on this point. Therefore, gnomonic distortion does not affect the measurement of a pure rotation w_{21} by means of Fourier-Mellin transform based cross-correlation (FMT-CC). However, computing the FMT involves here a polar resampling with a resolution of about 0.18° ($180^\circ/1024$ pixels). Consistently, an accuracy of 0.25° is obtained here in the presence of elastic strains of similar magnitude ($\varepsilon_{vm} = 5 \times 10^{-3}$ and 0.25° is close to 5×10^{-3} rad).

The error when the deformation is fully carried by a single elastic strain component with no rotation applied ($\Delta\theta = 0^\circ$) is plotted using colored

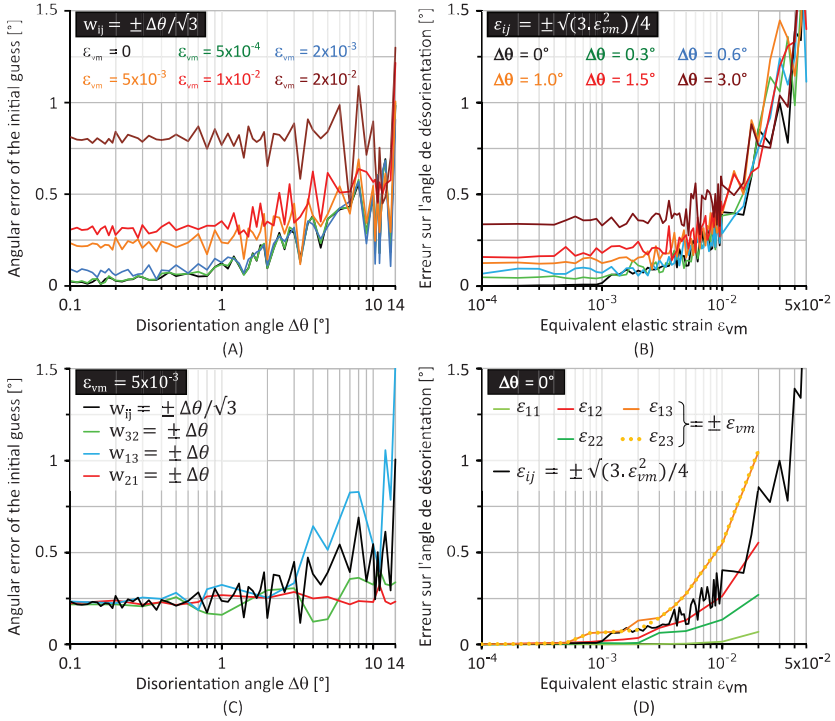


Fig. 3 Angular error of the global cross-correlation based initial guess as a function of (A) the disorientation angle $\Delta\theta$ and (B) the equivalent elastic strain ε_{vm} , when distributed between the different component. Angular error as a function of (C) $\Delta\theta$ when $\varepsilon_{vm} = 5 \times 10^{-3}$ and (D) of ε_{vm} when $\Delta\theta = 0^\circ$, when considering extreme cases (rotation or deformation carried by a single component).

lines in Fig. 3D. The black curve is just the same than previously in Fig. 3B. It is framed by the error associated with the extreme cases, which is also the case in Fig. 3C by the way. Once again, the influence of the PC location explains the discrepancies in the error as a function of ε_{vm} when a pure dilatation ε_{11} or ε_{22} is applied (green curves). Their effect is a horizontal or a vertical displacement gradient, respectively. The resulting translation of the displacement field at the subset scale is zero provided the PC coincides with the geometric center of the subset. It is not the case here. The larger the dilatation applied, the longer the resulting translation. Which is perceived as a rotation. The angular error thus increases with ε_{vm} . In addition, the PC being more vertically eccentric than horizontally, the latter increase is faster regarding ε_{22} (dark green curve) than regarding ε_{11} (light green curve).

Pure shear ε_{13} or ε_{23} (orange curves in Fig. 3D) roughly shifts patterns like rotations w_{13} and w_{23} do (see Fig. 9 in Chapter “Measuring elastic strains and orientation gradients by scanning electron microscopy: Conventional and emerging methods” by Ernould et al.). However, applying one or the other rotation gives a similar error in Fig. 3C, as long as the disorientation angle is lower than $\sim 3^\circ$. Consistently, no noticeable difference in error is observed between ε_{13} or ε_{23} since the maximum elastic strain applied is 2×10^{-2} , which in radians corresponds to 1.15° . It is therefore no coincidence that the angular error is about 1° .

Overall, it is necessary to step back from the observed error. The primary goal of the propose initial guess is to pre-align the patterns. The present observations testify to its tendency to capture the effects of elastic strains and to interpret them wrongly as rotations. Beyond the angular error, the convergence speed of the IC-GN algorithm must be studied.

3.2.3 Convergence speed of the IC-GN algorithm

The first goal of the global cross-correlation approach is to pre-align patterns so that the IC-GN algorithm converges rapidly. The number of iterations after a partial or complete initialization of the homography is shown in Fig. 4A,B, which is related to Fig. 3A,B. Regarding the complete initialization, the number of iterations is indicated by colored curves associated with the different elastic strain states (Fig. 4A) or disorientation angles (Fig. 4B) studied. The deviations between the curves correlate with those previously observed on the disorientation angle between the initial estimate and the solution (Fig. 3A,B). In comparison, the number of iterations following a partial initialization is represented by a red area bounded by the minimum and maximum observed among all cases.

A complete initialization of the homography ensures a convergence of the IC-GN algorithm in less than 30 iterations in most cases. Between 3 and 11 iterations are typically required for the most usual disorientation and elastic strain levels, namely $\Delta\theta \in [0; 3^\circ]$ and $\varepsilon_{vm} \leq 5 \times 10^{-3}$. On the contrary, a partial initialization results in a fast increase in the number of iterations as soon as the disorientation exceeds 2° (Fig. 4A). This is directly related to the higher values of the initial residuals, as illustrated in fig. 13c' in Chapter “Implementing the homography-based global HR-EBSD/TKD approach” by Ernould et al. The assumption of a rigid transformation of the target subset becomes too coarse beyond $7\text{--}8^\circ$ of disorientation. Indeed, the IC-GN algorithm starts to diverge, except in the case of a w_{21} rotation. As mentioned in the previous section, its measurement is not affected by gnomonic distortions.

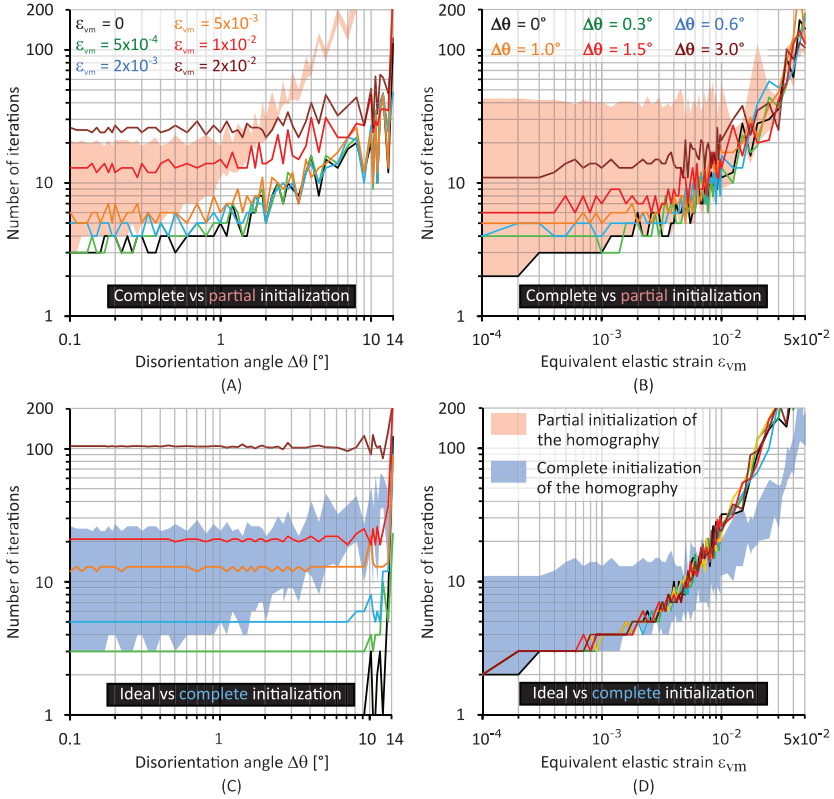


Fig. 4 (A, B) Number of iterations after a partial (red regions) or complete (colored curves) initialization of the homography as a function of (A) the disorientation angle and (B) the equivalent elastic strain. (C, D) Number of iterations when the rotations are a priori known in an exact way (colored curves) compared with the complete initialization of the homography (blue regions) as a function (C) of the disorientation angle or (D) of the equivalent elastic strain.

To better judge the performance of the method, an “ideal” initial guess is considered. The target subset is warped at the beginning of the IC-GN algorithm according to the exact rotations. The number of iterations is represented by the colored curves in Fig. 4C,D while the blue areas report the minimum and maximum number of iterations after a complete initialization (determined from the colored curves in the Fig. 4A,B).

As already discussed, the pattern pre-alignment method detects global displacements caused by elastic strains. Patterns subject to an equivalent elastic strain greater than $\sim 1\%$ are thus better pre-aligned than after an “ideal” initial guess. At low elastic strains ($\epsilon_{vm} \leq 2 \times 10^{-3}$), both the ideal and the

complete initialization result in a very similar number of iterations as long as the disorientation is less than one degree. Then, an “ideal” initialization unsurprisingly leads to a higher numerical efficiency of the IC-GN algorithm. When an initial guess disoriented by 0.1° or 0.5° is prescribed (not shown here), 6–8 and 20–50 iterations are necessary, respectively. This is in line with the proposed method.

3.3 Variability of the results

Following the discussion in Chapter “Implementing the homography-based global HR-EBSD/TKD approach” by Ernould et al., the influence of the convergence criterion and of a median or Gaussian spatial filter on the IC-GN algorithm are now investigated in terms of accuracy and number of iterations.

3.3.1 Relevance of the convergence criterion

More than 200 iterations are often required at the highest disorientations ($13\text{--}14^\circ$) in Fig. 4 ($C_{conv}=0.001$ pixel). However, this also concerns the case of an “ideal” initial guess. A slow convergence cannot thus be attributed to the pattern pre-alignment method alone. The sudden increase of the number of iterations takes place as the target subset goes out the pattern. The introduction of noise for the concerned pixels may be the reason. Slow convergence issues are not a priority at this stage of development, especially since the IC-GN algorithm converges to the expected solution (Fig. 2). The relevance of the convergence criterion C_{conv} is nevertheless checked. The previous dataset (optical distortion-free, fixed projection geometry) is re-analyzed by considering an “ideal” initial guess and different values of C_{conv} :

- 0,1 pixel (expected to be not restrictive enough).
- 0,01 pixel (minimum recommended by (Pan, 2014)).
- 0,001 pixel (chosen according to the literature).

The number of iterations is plotted as a function of the disorientation angle in the case where $\epsilon_{vm}=2 \times 10^{-2}$ in Fig. 5A. The observed trend is nevertheless representative of the other cases. In addition, the number of iterations is plotted as a function of equivalent elastic strain in Fig. 5B. Since the disorientation angle has a marginal influence, as shown by the colored curves in Fig. 4D, only the average of the six cases is displayed. As expected, the IC-GN algorithm converges often prematurely when C_{conv} is 0.1 pixel (red dashed lines). This is accompanied by maximum errors much larger than 1×10^{-4} in Fig. 5C,D. In contrast, the error is typically less than

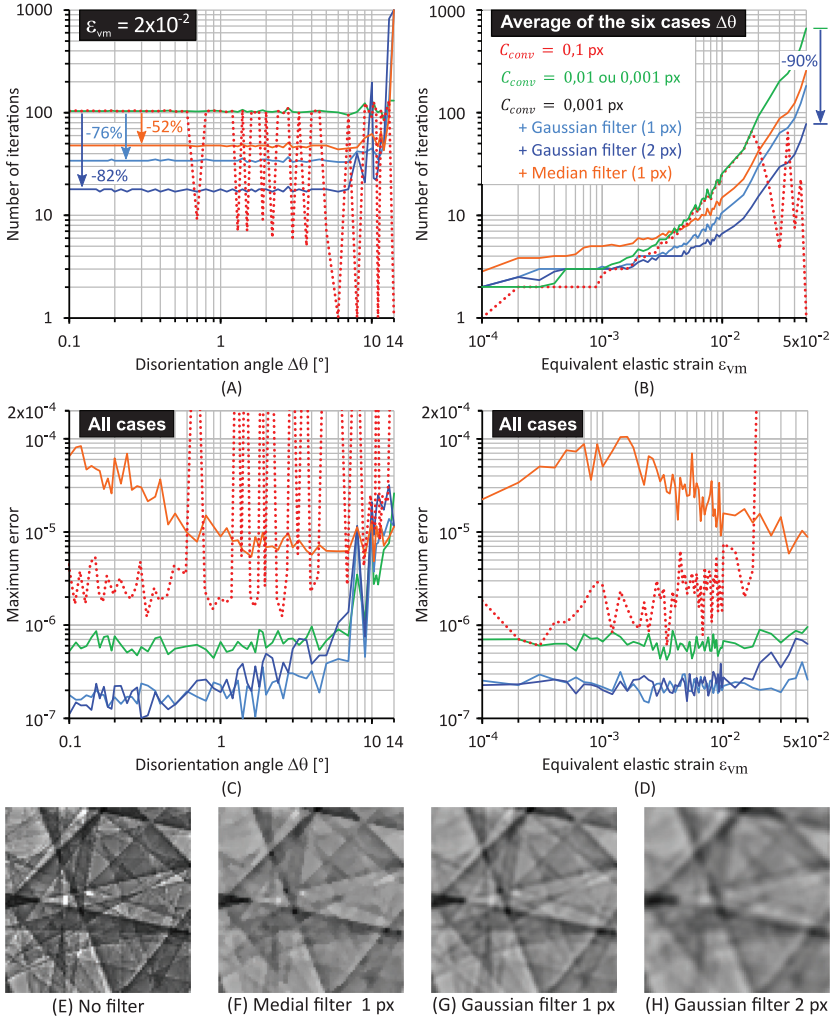


Fig. 5 Results obtained without pattern filtering for different convergence criterion C_{conv} or after applying a spatial filter while considering $C_{conv} = 0.001$ pixel. (A, B) Number of iterations and (C, D) maximum error as a function of (A, C) the disorientation angle and (B, D) the equivalent elastic strain. Detail of 80×80 pixels of a pattern (E) with no filtering, (F) after a median filter of radius 1 pixel, (G) after a Gaussian filter of radius 1 pixel, (H) after a Gaussian filter of radius 2 pixels.

1×10^{-6} for a convergence criterion of 0.01 pixel or 0.001 pixel, with a maximum of $\sim 1 \times 10^{-5}$ for disorientations greater than 10° . These two C_{conv} values lead to quasi-identical results, so they are represented by the same green curve. A convergence criterion of 0.001 pixel appears as a

suitable choice, meaning that recommendations from the literature considering subsets of a few tens of pixels size are transferable to larger subsets.

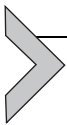
3.3.2 Influence of a median or Gaussian spatial filter

In anticipation of the application of the method to experimental images, the influence of a median or Gaussian filter on accuracy and convergence speed is studied ($C_{conv} = 0.001$ pixel).

A median filter based on the four nearest neighbors is applied. Its effect is illustrated from a 80×80 pixel detail in Fig. 5F, which is to be compared to the original detail in Fig. 5E. Taking the unfiltered case as a reference (green curves in Fig. 5), the application of a median filter (orange curve) reduces the number of iterations by about 50% at large elastic strains (2% in Fig. 5A) but increases it by 1 or 2 iterations at smaller levels (Fig. 5B). The main shortcoming of this filter is the increase of the error by one order of magnitude as compared to in the absence of filtering in Fig. 5C,D (but it nevertheless remains below $\sim 1 \times 10^{-4}$).

Conversely, a Gaussian filter with a radius of one pixel (light blue curves, detail Fig. 5G) or two pixels (dark blue curves, detail Fig. 5H) is accompanied by a reduction in the maximum error, except at large disorientations. Compared to the unfiltered case, a Gaussian filter with a radius of two pixels can reduce the number of iterations by 90%, without loss in accuracy.

These observations relativize the slow convergence issues observed. They highlight the need to further study the definition of convergence and to identify factors impacting the numerical efficiency of the IC-GN algorithm as discussed in Chapter “Implementing the homography-based global HR-EBSD/TKD approach” by Ernould et al.



4. Necessity of a correction of optical distortions

The error made when neglecting first-order radial distortion is first quantified, as well as the influence of the position of the PC and of the optical center. Then, the necessity of a correction of optical distortions, even at small disorientation angles is demonstrated. Finally, the accuracy on the correction parameters ensuring the effectiveness of the correction is evaluated.

4.1 Error in the absence of a correction

4.1.1 Influence of the coefficient of distortion

The ten datasets subject to different K_1 values from Section 3.1 are re-analyzed while disabling the correction. The maximum error with and

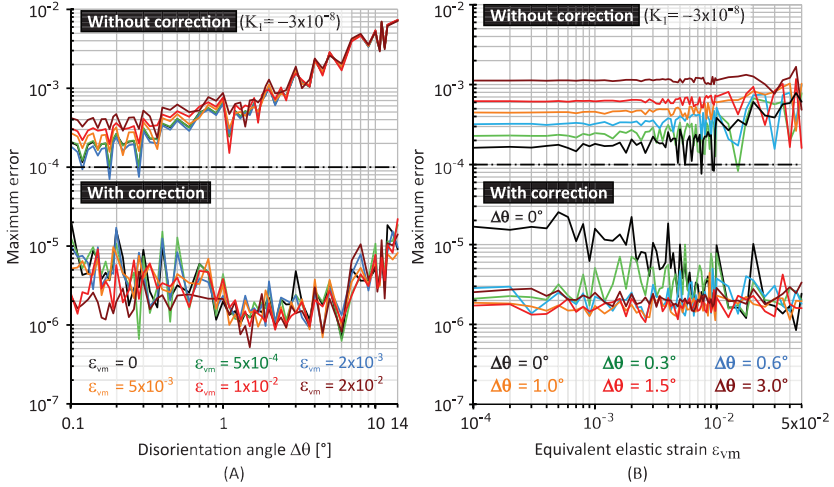


Fig. 6 Comparison of the maximum error obtained with and without correction in the case $K_1 = -3 \times 10^{-8}$. Maximum error as a function of (A) the disorientation angle and (B) the equivalent elastic strain.

without correction is compared in Fig. 6 in the case $K_1 = -3 \times 10^{-8}$. While the correction keeps the error below $\sim 2 \times 10^{-5}$, it exceeds $\sim 1 \times 10^{-4}$ otherwise. In other words, an optical distortion typical of EBSD camera is sufficient to induce larger errors than the commonly claimed accuracy of the HR-EBSD/TKD technique under suitable experimental conditions.

Without correction, the error increases rapidly with the disorientation angle in Fig. 6A, which is also visible by the clear “stacking” of the curves in Fig. 6B where $\varepsilon_{vm} \leq 5 \times 10^{-3}$. Conversely, the error is little affected by the level of elastic strain. No clear trend is observed between the six elastic strain states studied in Fig. 6A while curves are relatively flat in Fig. 6B.

The absence of correction is accompanied by oscillations in the error. Visually, it is also the case with correction, but the order of magnitude is much smaller. The homography is not able to describe faithfully the displacement field between the distorted images. The IC-GN algorithm then probably converges to a local optimum of the similarity criterion. As the displacements are mainly imposed by rotations, these oscillations are particularly visible in Fig. 6A, especially at large disorientations. Concerning Fig. 6B, the oscillations become noticeable from the moment displacements caused by elastic strain equal those of rotations. For example, the black curve ($\Delta\theta = 0^\circ$) clearly oscillates from $\varepsilon_{vm} \geq \sim 5 \times 10^{-3}$, which in radians is about 0.3° .

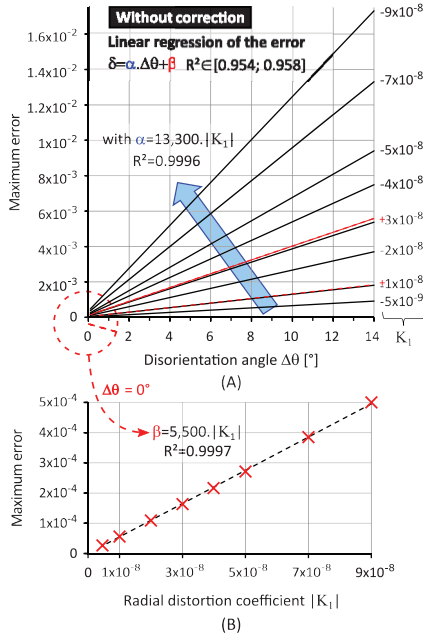


Fig. 7 (A) Linear regression of the error as a function of the disorientation angle when neglecting a first-order radial distortion of coefficient K_1 . (B) Linear regression of the intercept of the error (i.e., the error at $\Delta\theta = 0^\circ$) as a function of the absolute value of the distortion coefficient K_1 .

The trends observed for $K_1 = -3 \times 10^{-8}$ also apply to the other nine datasets. Since the error slightly depends on elastic strains, the average error of the six studied deformation states is computed and its linear regression with respect to the disorientation angle is plotted in Fig. 7A., i.e., $E = \alpha \cdot \Delta\theta + \beta$. The coefficient of determination R^2 is between 0.954 and 0.958 depending on the dataset. In addition, the slope α and the intercept β are both proportional to K_1 in absolute value ($R^2 > 0.999$), as highlighted in Fig. 7B regarding β . Neglecting a barrel ($K_1 < 0$) or a pincushion ($K_1 > 0$) radial distortion consequently leads to the same level of error, as shown by the red dash-lines in Fig. 7A.

As a conclusion, neglecting a first-order radial distortion of coefficient K_1 lying between -2×10^{-8} to -4×10^{-8} , which is typical of EBSD cameras (Mingard et al., 2011), results in error of the order 1 to 5×10^{-3} .

4.1.2 Influence of the PC and optical center locations

The influence of the position of the PC and of the optical center on the error (without correction) is studied through six datasets designated by the letters A to F in Fig. 8. They are generated by applying a radial distortion

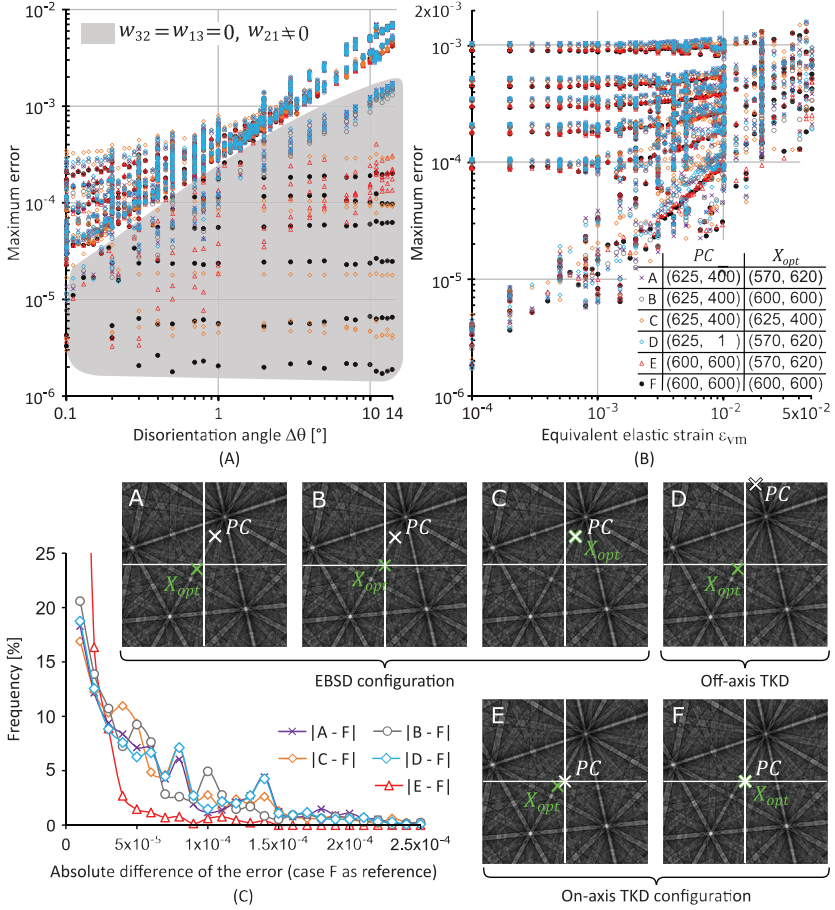


Fig. 8 Maximum error in the absence of correction for different PC and optical center positions (absolute coordinates in the table). Maximum error as a function of (A) the disorientation angle and (B) the equivalent elastic strain. (C) Distribution of the absolute deviations in error between the maximum errors obtained for a dataset and those for configuration F.

of coefficient $K_1 = -3 \times 10^{-8}$ and considering a fixed projection geometry ($\delta PC = 0$). The position of the PC is chosen to be representative of the EBSD (cases A, B, C), the off-axis TKD (case D) and the on-axis TKD (cases E and F) configurations. The absolute coordinates of the optical center and of the PC are specified in the table in Fig. 8B. As a reminder, the size of the pattern is 1200×1200 pixels.

Errors associated with all configurations are more or less superimposed in Fig. 8A,B, meaning the PC position is not a determining factor. To better

quantify differences between configurations, their respective error is compared to that of configuration F (i.e., PC and optical center coinciding with the center of the image). The distributions in Fig. 8C show the difference in error between configurations is essentially less than 1.5×10^{-4} .

The main differences in error concern the cases where the rotations w_{32} and w_{13} are simultaneously zero, which are included within the gray region in Fig. 8A. They stand out because a pure (in-plane) rotation w_{21} is perfectly measurable without correction if the PC coincides with the optical center. Errors lower than 1×10^{-5} are thus observed for configurations C and F (orange diamonds and black disks, respectively). Conversely, the upper edge of the gray region is delimited by the configuration A, B and D (blue and gray markers), whose the distance between the PC and the optical center is higher.

Apart from the specific case $w_{32} = w_{13} = 0$, the error when neglecting first-order radial distortion is marginally affected with the PC and optical center positions. Therefore, errors as a function of K_1 and $\Delta\theta$ presented in Fig. 7A (configuration A) are generalizable.

4.2 Relative error on rotation and elastic strain components

The importance of optical distortions for accurate HR-EBSD/TKD measurements was discussed in Chapter “Measuring elastic strains and orientation gradients by scanning electron microscopy: Conventional and emerging methods” by Ernould et al. (section 3.3). Provided the reference and target patterns are distorted in the same way, as it is the case here, (Britton et al., 2010) argued that neglecting a first-order radial distortion was acceptable in the presence of rotations lower than 2.5° . The present results indicate the opposite.

An accuracy of $\sim 1 \times 10^{-4}$ cannot be guaranteed (Fig. 6) and the error even reaches $\sim 8 \times 10^{-4}$ at “only” 1° of disorientation, when neglecting a radial distortion of coefficient $K_1 = -3 \times 10^{-8}$. This agrees with the error of 6.1×10^{-4} on elastic strain components reported by Britton et al. (2010).

Based on Fig. 7A, this value is nevertheless quite small given that a distortion of 10^{-7} was applied. Actually, only particular cases were investigated by Britton et al. (2010): an elastic strain-free state subject to pure rotation with respect to the normal of the sample. Granted, the latter does not coincide with the scintillator’s normal, so patterns are not subject to a pure in-plane rotation, but the transformation remain quite similar. As highlighted by the gray area in Fig. 8A, the error in such test conditions is likely to be underestimated as compared to a more randomly chosen ones.

However, the main disagreement concerns the relative error. According to (Britton et al., 2010), it is about $\sim 1.5\%$ of the value applied, which is marginal. This statement seems insidious to the present authors since it does not correspond to the usual definition of the relative error. This value was obtained by dividing the error on elastic strain components by the applied rotation, namely 2.5° or 4.4×10^{-2} rad. Note that this rotation was the onliest non-zero component, meaning relative error on elastic strains is logically undefined (or infinite). Given the noise floor was about 1×10^{-4} , a solution might have been to consider that obtaining 6.1×10^{-4} instead of zero is a relative error of 600%.

Considering the results without correction in Fig. 6, the maximum relative error is computed according to Eq. (12) and plotted in Fig. 9A,B. The cases $\Delta\theta = 0^\circ$ and $\varepsilon_{vm} = 0$ are omitted because many components are zero,

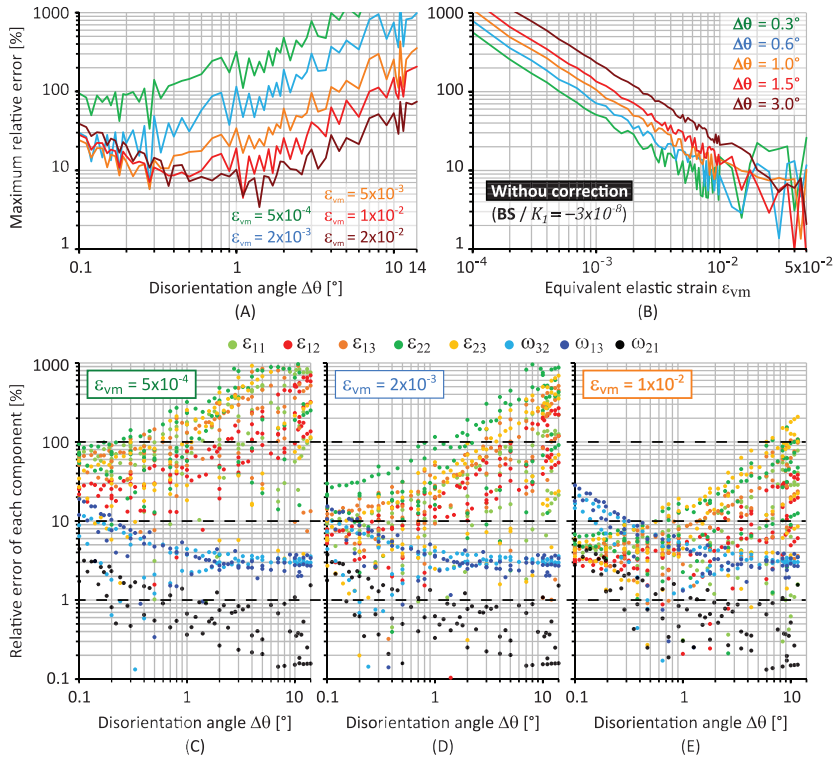


Fig. 9 Maximum relative error as a function of (A) the disorientation angle and (B) the equivalent elastic strain when radial distortion of coefficient $K_1 = -3 \times 10^{-8}$ is neglected. Relative error on each elastic strain or rotation component as a function of the disorientation angle when the equivalent elastic strain is (C) 5×10^{-4} , (D) 2×10^{-3} , (E) 1×10^{-2} .

biasing the comparison with the other curves. The maximum relative error is typically several tens of percent. It increases with the disorientation angle and decreases with the equivalent elastic strain. For elastic strains of the order of 10^{-4} , the relative error exceeds 100%. It even reaches 1000% depending on the disorientation angle (Fig. 9B), which is consistent with the value of 600% deduced from (Britton et al., 2010). Correcting optical distortions thus appears necessary for any accurate measurement of rotations and elastic strains, no matter the disorientation angle is small or the patterns are distorted in the same way.

The relative error on each of the elastic strain or rotation components (non-zero in input) is plotted for the case $\varepsilon_{vm} \approx 5 \times 10^{-4}$ (Fig. 9C), $\sim 2 \times 10^{-3}$ (Fig. 9D) and $\sim 1 \times 10^{-2}$ (Fig. 9E). In general, the elastic strain components are more affected by optical distortions than are the rotation components. This observation nevertheless reverses as soon as the displacements generated by the elastic strains become preponderant. Fig. 9E shows that in the case of $\varepsilon_{vm} = 1\%$, the maximum relative error at low disorientations is imposed by the relative error on rotations (blue points) and no longer by the one on elastic strains. This explains the increase of the maximum relative error for $\varepsilon_{vm} \geq 5 \times 10^{-3}$ at disorientations lower than $\sim 0.3^\circ$ ($\sim 5 \times 10^{-3}$ rad) in Fig. 9A (orange, red, and brown curves).

4.3 Required accuracy of the distortion model parameters

In practice, the distortion model implemented in the correction approximates the true optical distortion effects. Here, the correction is assumed effective if the maximum error does not exceed 1×10^{-4} . Based on this, the required accuracy on the position of the optical center and on the value of the distortion coefficient K_1 is evaluated. The study focuses on angular disorientations less than 3° since accurate measurement of elastic deformations is usually limited to slightly plastically deformed metals or purely elastically deformed semiconductors.

The PC and optical center locations showing little influence on the maximum error in Section 4.1.2, only configuration A (Fig. 8) is considered. As a reminder, it is representative of EBSD cameras. Calculations were performed using erroneous values for the absolute coordinates of the optical center ($\mathbf{X}_{opt} = [570 \ 620]^T$) and/or of the distortion coefficient $K_1 = -3 \times 10^{-8}$. Fig. 10 gathers the most relevant results. Note that errors greater than $\sim 2 \times 10^{-5}$ are attributable to optical distortion according to the numerical validation (Fig. 2C,D).

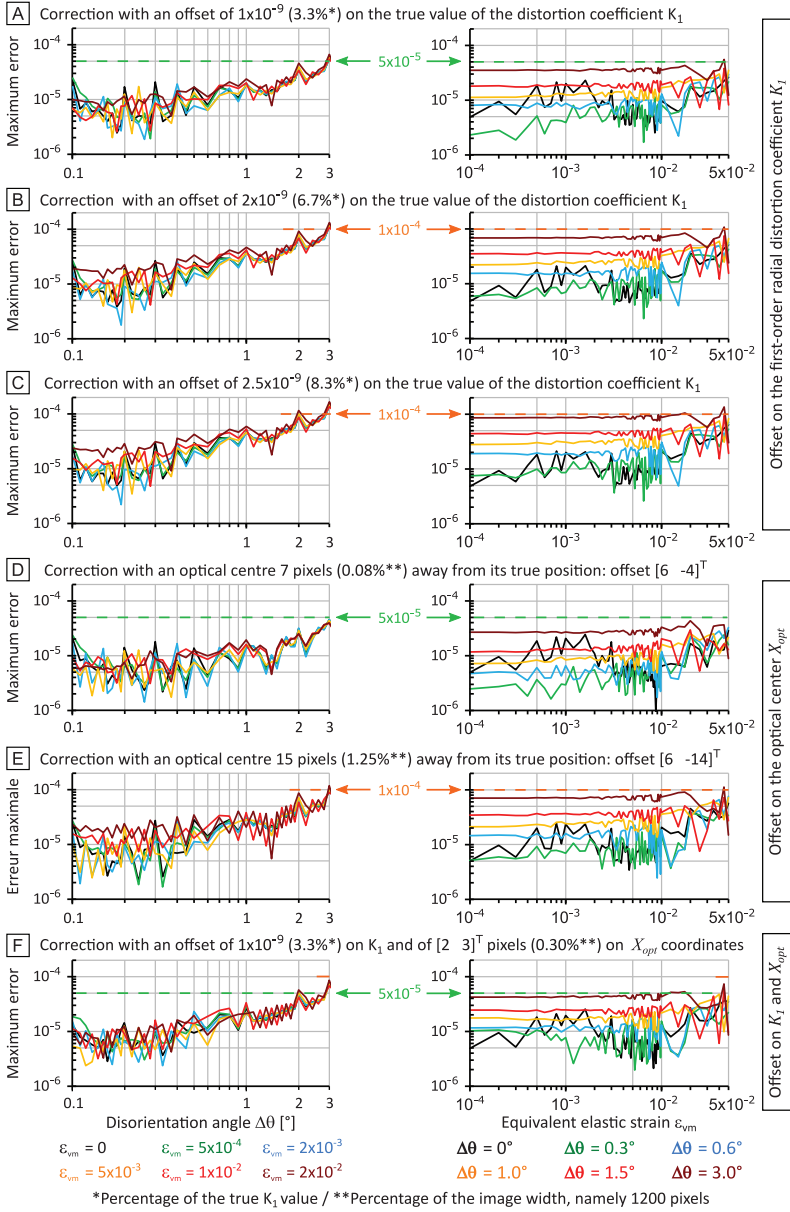
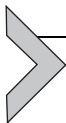


Fig. 10 Maximum error when erroneous parameters are prescribed to the first-order radial distortion model involved in the correction ($K_1 = -3 \times 10^{-8}$ applied).

When the optical center is correct, an accuracy of $\pm 1 \times 10^{-9}$ on K_1 appears sufficient, the maximum error remaining below $\sim 5 \times 10^{-5}$ up to 3° of disorientation in Fig. 10A. The error reaches $\sim 1 \times 10^{-4}$ at disorientations higher than $\sim 6.5^\circ$ (not shown here). However, such an error is already observed from 3° of disorientation for uncertainties between $\pm 2 \times 10^{-9}$ (Fig. 10B) and $\pm 2.5 \times 10^{-9}$ (Fig. 10C). Actually, an error of δK_1 on the coefficient K_1 induces the same error as if a radial distortion of coefficient δK_1 was neglected. The accuracy of $\pm 1 \times 10^{-9}$ required here is thus not specific to the present K_1 value.

When K_1 is correct, the error remains below $\sim 5 \times 10^{-5}$ as long as the prescribed optical center is not more than ~ 7 pixels away from its true position (Fig. 10D). At 3° of disorientation, the maximum error is $\sim 1 \times 10^{-4}$ for ~ 15 pixels error in the optical center position (Fig. 10E).

When the optical center and the distortion coefficient are simultaneously erroneous, an uncertainty of 1–3 pixels in the true position of the optical center and an uncertainty of $\pm 1 \times 10^{-9}$ in the K_1 coefficient are acceptable. As shown in Fig. 10F, the maximum error does not exceed 1×10^{-4} and remains essentially below $\sim 5 \times 10^{-5}$.



5. Discussion

This chapter confirms numerically that a linear homography describes the displacement on the scintillator sought by the HR-EBSD/TKD technique. The working principle of the optical distortion correction integrated in the IC-GN algorithm is also validated.

Errors are particularly low when optical distortions are properly corrected or simply absent. However, they are not intended to be compared with those of other studies, especially since the images are not individual dynamical simulations. As detailed in Section 2.2, some diffraction effects have not been reproduced. However, they do not constitute an obstacle to the numerical validation of the method. On the one hand, the approach is supported by previous works like (Vermeij & Hoefnagels, 2018). On the other hand, it enables to pay particular attention to interpolation bias. Actually, its influence is at least as important as the diffraction effects absent from the test images used.

As shown in Fig. 2, interpolation bias can limit accuracy to $\sim 1 \times 10^{-4}$ in the presence of elastic strains representative of metals ($\epsilon_{vm} \leq \sim 2 \times 10^{-3}$) and rotations of a few tenths of a degree ($\Delta\theta \leq 0, 3^\circ$), namely in the typical

application conditions of the HR-EBSD/TKD technique. Interestingly, such a level of error agrees with the error of 1 to 2×10^{-4} obtained from dynamically simulated patterns by (Britton & Wilkinson, 2012) and (Ruggles et al., 2018), who used bicubic and cubic B-splines interpolation, respectively. Still using dynamically simulated patterns, errors as low as 2×10^{-5} and typically worth 5×10^{-6} are reported by Maurice et al. (2012) and Vermeij and Hoefnagels (2018), respectively. Unfortunately, the interpolation scheme is not specified.

First raised by Maurice, Dzieciol, and Fortunier (2011), the question of the interpolation scheme is becoming increasingly inevitable since the introduction of the remapping technique (Britton & Wilkinson, 2012; Maurice et al., 2012; Zhu, Kaufmann, & Vecchio, 2020) and of global HR-EBSD/TKD approaches (Ernould, Beausir, Fundenberger, Taupin, & Bouzy, 2020a; Ruggles et al., 2018; Shi et al., 2019; Vermeij, De Graef, & Hoefnagels, 2019; Vermeij & Hoefnagels, 2018). The question of the optimal interpolation scheme for the HR-EBSD technique remains open. (Ruggles et al., 2018) noted that biquintic B-splines do not provide an accuracy gain compared to cubic B-splines with lower numerical cost. As mentioned in Chapter “Development of a homography-based global DIC approach for high-angular resolution in the SEM” by Ernould et al., the IC-GN algorithm was chosen because it benefits from a large literature. Recently, (Su et al., 2019) proposed a method for removing systematic errors due to interpolation. It consists of applying random shifts on the positions to be interpolated during the FA-GN (Forward-additive Gauss-Newton) or IC-GN algorithm.

By minimizing errors due to interpolation bias, the present study allows small errors of the order of 1×10^{-4} or less caused by uncorrected or improperly corrected optical distortions to be quantify, especially in Fig. 10.

By avoiding time-consuming simulations, thousands of tests conditions could be analyzed in a reasonable time. This is an important point that is sometimes overlooked in the literature. Care should be taken to ensure that the DIC algorithms are able to account for all necessary displacements or displacement gradients that may occur between the reference and the target pattern. As an example, (Ruggles et al., 2018) validated a global HR-EBSD/TKD method also employing an IC-GN algorithm from dynamically simulated patterns, but without including shear of the lattice cell. As detailed in Section 4.2 regarding the necessity of a correction of optical distortions, wrong conclusions may be drawn from few cases, especially if simple rotations or elastic strains states are applied.

More generally, the HR-EBSD/TKD community would benefit from having a common bank of simulated or experimental patterns. In this spirit, (Shi et al., 2019) experimentally validated their method by reusing the data from (Plancher et al., 2016) in a single crystal of austenitic 316L steel in 4-point bending.

Regarding the global cross-correlation based initial guess, it fulfilled its purpose since the IC-GN algorithm converges in less than ~ 10 iterations in the presence of moderate disorientation and elastic strains ($\Delta\theta \leq 3^\circ$ and $\varepsilon_{vm} \leq 5 \times 10^{-3}$) and in less than ~ 30 iterations for other cases (ignoring the few cases of slow convergence). These values are obtained with a complete initialization of the homography. As expected, convergence after a partial initialization is limited to moderate disorientations ($< 7^\circ$) in the case of a projection geometry typical of the EBSD configuration (Fig. 4A,B). Note that applications to EBSD and on-axis TKD patterns are intended in this work, so the pre-alignment method is not particularly designed for off-axis TKD patterns, for which asymmetry of gnomonic distortion is significant along the vertical direction.

The relevance of the convergence criterion, $C_{conv} = 0.001$ pixel is confirmed (Fig. 5), although slow convergence is sometimes observed. It seems related to implementation details since the same issue occurs even when the initial guess is “ideal” (homography initialized from the exact rotations). The number of iterations is also highly dependent on spatial filters (up to 90% reduction when applying a Gaussian filter of radius 2 pixels), echoing similar observations from experimental patterns by (Shi et al., 2019). The latter authors explain that a Gaussian filter reduces the high frequencies associated with noise, which impair convergence speed. The introduction of noise for points outside the target pattern therefore seems inappropriate. This implementation aspect has not been optimized, at this stage of development as it concerns very few cases in practice.

The robustness of the IC-GN algorithm against noise can be improved using errors functions, which weight pixels according to their residuals (Sánchez, 2016). However, the Hessian matrix must then be recomputed at each iteration, like in the FA-GN algorithm. In this case, the numerical efficiency of the IC-GN algorithm is strongly affected but it is still advantageous as compared to the FA-GN algorithm because of the Hessian-matrix evaluation at $\mathbf{p} = \mathbf{0}$. Recently, (Shi et al., 2021) proposed a calibration technique of EBSD patterns, which involves weights in the DIC algorithms. They notably highlighted readout artifacts of the charge coupled device.

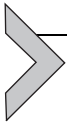
Concerning optical distortion, errors made by neglecting a first-order radial distortion increases linearly with the absolute value of the distortion coefficient K_1 as well as with the disorientation angle. This linear relationship, already highlighted by Britton et al. (2010), is known in the literature. It is precisely used to estimate K_1 from the DIC measurement error on the displacement of a sight translated using a stage (Pan, Yu, Wu, & Tang, 2013).

When neglecting a typical barrel distortion $K_1 = -3 \times 10^{-8}$ (Mingard et al., 2011), the error is between 1 and 5×10^{-3} in the presence of disorientations lower than 8° . The same order of magnitude is reported by (Britton et al., 2010) considering optically distorted target patterns and a distortion-free reference. Their conclusion regarding the case where all patterns are distorted in the same way is however contradicted by this study. On the one hand, the typical accuracy of 1×10^{-4} cannot be achieved when radial distortion of coefficient $K_1 = -3 \times 10^{-8}$ is neglected (Fig. 6). On the other hand, the relative error on the rotation or elastic strain components is much higher than 10%. They are only two specific situations, in which not accounting for optical distortion appears acceptable: when measuring elastic strains about 10^{-2} in the presence of disorientations of less than 1° or when considering exclusively rotations at disorientations higher than $\sim 0.5^\circ$ (Fig. 9).

Ideally, this study should be extended to more complex distortion models. Here, only first-order radial distortion is considered since it has a predominant effect (Drap & Lefèvre, 2016; Pan, Yu, Wu, & Tang, 2013; Wang et al., 2008) and because it admits an analytical inverse distortion model. It arises that the required accuracy on the position of the optical center and the first-order distortion efficient K_1 matches the resolution of the measurements in (Mingard et al., 2011). More specifically, locating the optical center within one or two pixels and determining K_1 within 1×10^{-9} is necessary so that the error remains below 1×10^{-5} in the presence of disorientations up to 3° (Fig. 10F). Optical distortions of EBSD camera should be more finely characterized to verify the extent to which tangential distortion or second-order radial distortion affect them and can be neglected or not.

Beyond a software solution, like the proposed correction, hardware improvements are also possible. The HR-EBSD technique would benefit from dedicated acquisition systems not limited to simply increasing the resolution and sensitivity of the camera. In addition to optical distortion, (Mingard et al., 2011) pointed out the lack of rigidity and repositioning precision of most camera mechanical insertion systems. They are a hindrance to accurate SEM calibration using the moving screen technique (Maurice et al., 2011;

Mingard et al., 2011). Optical distortions can also be greatly reduced by bilateral telecentric lenses, whose the interest for surface deformation measurement in experimental mechanics was showed by (Pan, Yu, & Wu, 2013). In addition, they lessen problems associated with camera self-heating (Ma, Pang, & Ma, 2012; Pan, Yu, & Wu, 2013). A more radical solution is to use optic-free devices. Therefore, EBSD cameras with a scintillator connected to the sensor using fiber-optic tapers have been commercialized for a few years.



6. Summary

6.1 Numerical validation of the method

- The homography-based global HR-EBSD/TKD approach and the integration of a correction of optical distortion in the IC-GN algorithm are validated numerically in the presence of disorientations up to 14° and equivalent elastic strains up to 5%.
- By minimizing the error sources during the generation of the test images, the present study highlights the influence of the interpolation bias on accuracy. It can limit the accuracy of the method to 1×10^{-4} when small rotations ($\leq 0.3^\circ$) and elastic strain ($\leq 2 \times 10^{-3}$) are present.
- The global cross-correlation based initial guess ensures the convergence of the IC-GN algorithm to the solution. However, a partial initialization of the homography is not recommended in the presence of disorientations greater than $\sim 7^\circ$.
- A value of 0.001 pixel for the convergence criterion C_{conv} is relevant, consistently with the literature (Pan, 2014; Pan, Li, & Tong, 2013; Shao et al., 2015; Zhang et al., 2015). However, slow convergence is sometimes observed at the largest disorientations ($> 11^\circ$). It is likely due to the introduction of noise, the initial guess being not in question. A study of factors influencing the convergence as well as the optimization of its definition is desirable, as discussed in Chapter “Implementing the homography-based global HR-EBSD/TKD approach” by Ernould et al.

6.2 Influence of optical distortion on accuracy

- The error made when neglecting a first-order radial distortion typical of EBSD cameras, i.e., $K_1 = -3 \times 10^{-8}$, (Mingard et al., 2011) is of the order of 10^{-3} but can reach 10^{-2} . This error increases linearly with the absolute

value of the distortion coefficient and with the disorientation angle. The equivalent elastic strain and the position of the PC have no significant influence.

- A correction of optical distortions is necessary to measure elastic strains accurately, even in the presence of small disorientations of a few tenths of a degree, and especially if they are in the typical range of metals (1×10^{-4} to 2×10^{-3}). Without a suitable correction, relative errors are likely to exceed 100%.
- Neglecting a radial distortion of $K_1 = -3 \times 10^{-8}$ leads to relative errors of less than 10% only for rotation components provided the disorientation angle is greater than $\sim 0.3^\circ$ or only for elastic strain components provided they are of the order of 1×10^{-2} and the disorientation angle is less than 1° .
- Considering $K_1 = -3 \times 10^{-8}$, accuracy of 1 to 3 pixels on the position of the optical center and $\pm 1 \times 10^{-9}$ on the first-order distortion coefficient ensures the effectiveness of the correction, i.e., the error is less than $\sim 5 \times 10^{-5}$ in the presence of disorientation up to 3° . In comparison with the projection geometry, the accuracy required on the parameters of the optical distortion model not seem to be as critical.

References

- Baker, S., & Matthews, I. (2004). Lucas-Kanade 20 years on: A unifying framework. *International Journal of Computer Vision*, 56(3), 221–255. <https://doi.org/10.1023/B:VISI.0000011205.11775.fd>.
- Bornert, M., Doumalin, P., Dupré, J.-C., Poilane, C., Robert, L., Toussaint, E., et al. (2017). Shortcut in DIC error assessment induced by image interpolation used for subpixel shifting. *Optics and Lasers in Engineering*, 91, 124–133. <https://doi.org/10.1016/j.optlaseng.2016.11.014>.
- Britton, T. B., Maurice, C., Fortunier, R., Driver, J. H., Day, A. P., Meaden, G., et al. (2010). Factors affecting the accuracy of high resolution electron backscatter diffraction when using simulated patterns. *Ultramicroscopy*, 110(12), 1443–1453. <https://doi.org/10.1016/j.ultramic.2010.08.001>.
- Britton, T. B., & Wilkinson, A. J. (2011). Measurement of residual elastic strain and lattice rotations with high resolution electron backscatter diffraction. *Ultramicroscopy*, 111(8), 1395–1404. <https://doi.org/10.1016/j.ultramic.2011.05.007>.
- Britton, T. B., & Wilkinson, A. J. (2012). High resolution electron backscatter diffraction measurements of elastic strain variations in the presence of larger lattice rotations. *Ultramicroscopy*, 114, 82–95. <https://doi.org/10.1016/j.ultramic.2012.01.004>.
- Drap, P., & Lefèvre, J. (2016). An exact formula for calculating inverse radial Lens distortions. *Sensors (Basel, Switzerland)*, 16(6). <https://doi.org/10.3390/s16060807>.
- Ernould, C. (2020). *Développement et application d'une méthode à haute résolution angulaire pour la mesure des gradients d'orientation et des déformations élastiques par microscopie électronique à balayage* (These de doctorat, Université de Lorraine) <http://www.theses.fr/2020LORR0225>.

- Ernould, C., Beausir, B., Fundenberger, J.-J., Taupin, V., & Bouzy, E. (2020a). Global DIC approach guided by a cross-correlation based initial guess for HR-EBSD and on-axis HR-TKD. *Acta Materialia*, *191*, 131–148. <https://doi.org/10.1016/j.actamat.2020.03.026>.
- Ernould, C., Beausir, B., Fundenberger, J.-J., Taupin, V., & Bouzy, E. (2020b). Characterization at high spatial and angular resolutions of deformed nanostructures by on-axis HR-TKD. *Scripta Materialia*, *185*, 30–35. <https://doi.org/10.1016/j.scriptamat.2020.04.005>.
- Ernould, C., Beausir, B., Fundenberger, J.-J., Taupin, V., & Bouzy, E. (2021). Integrated correction of optical distortions for global HR-EBSD techniques. *Ultramicroscopy*, *221*, 113158. <https://doi.org/10.1016/j.ultramic.2020.113158>.
- Hartley, R., & Zisserman, A. (2004). Projective geometry and transformations of 2D. *Multiple View Geometry in Computer Vision*. <https://doi.org/10.1017/CBO9780511811685.005>.
- Ma, S., Pang, J., & Ma, Q. (2012). The systematic error in digital image correlation induced by self-heating of a digital camera. *Measurement Science and Technology*, *23*(2), 025403. <https://doi.org/10.1088/0957-0233/23/2/025403>.
- Maurice, C., Driver, J. H., & Fortunier, R. (2012). On solving the orientation gradient dependency of high angular resolution EBSD. *Ultramicroscopy*, *113*, 171–181. <https://doi.org/10.1016/j.ultramic.2011.10.013>.
- Maurice, C., Dzieciol, K., & Fortunier, R. (2011). A method for accurate localisation of EBSD pattern centres. *Ultramicroscopy*, *111*(2), 140–148. <https://doi.org/10.1016/j.ultramic.2010.10.007>.
- McLean, M. J., & Osborn, W. A. (2018). In-situ elastic strain mapping during micro-mechanical testing using EBSD. *Ultramicroscopy*, *185*, 21–26. <https://doi.org/10.1016/j.ultramic.2017.11.007>.
- Mingard, K., Day, A., Maurice, C., & Quedest, P. (2011). Towards high accuracy calibration of electron backscatter diffraction systems. *Ultramicroscopy*, *111*(5), 320–329. <https://doi.org/10.1016/j.ultramic.2011.01.012>.
- Pan, B. (2014). An evaluation of convergence criteria for digital image correlation using inverse compositional gauss-newton algorithm. *Strain*, *50*(1), 48–56. <https://doi.org/10.1111/str.12066>.
- Pan, B., Li, K., & Tong, W. (2013). Fast, robust and accurate digital image correlation calculation without redundant computations. *Experimental Mechanics*, *53*(7), 1277–1289. <https://doi.org/10.1007/s11340-013-9717-6>.
- Pan, B., Yu, L., & Wu, D. (2013). High-accuracy 2D digital image correlation measurements with bilateral Telecentric lenses: Error analysis and experimental verification. *Experimental Mechanics*, *53*(9), 1719–1733. <https://doi.org/10.1007/s11340-013-9774-x>.
- Pan, B., Yu, L., Wu, D., & Tang, L. (2013). Systematic errors in two-dimensional digital image correlation due to lens distortion. *Optics and Lasers in Engineering*, *51*(2), 140–147. <https://doi.org/10.1016/j.optlaseng.2012.08.012>.
- Plancher, E. (2015). *Mesures de champs de déformations élastique et totale pour la détermination du comportement mécanique local de matériaux cristallins* (These de doctorat, Paris, ENSAM) <https://www.theses.fr/2015ENAM0056>.
- Plancher, E., Petit, J., Maurice, C., Favier, V., Saintoyant, L., Loinsard, D., et al. (2016). On the accuracy of elastic strain field measurements by Laue microdiffraction and high-resolution EBSD: A cross-validation experiment. *Experimental Mechanics*, *56*(3), 483–492. <https://doi.org/10.1007/s11340-015-0114-1>.
- Ruggles, T. J., Bomarito, G. F., Qiu, R. L., & Hochhalter, J. D. (2018). New levels of high angular resolution EBSD performance via inverse compositional gauss-Newton based digital image correlation. *Ultramicroscopy*, *195*, 85–92. <https://doi.org/10.1016/j.ultramic.2018.08.020>.
- Sánchez, J. (2016). The inverse compositional algorithm for parametric registration. *Image Processing On Line*, *6*, 212–232. <https://doi.org/10.5201/ipol.2016.153>.

- Shao, X., Dai, X., & He, X. (2015). Noise robustness and parallel computation of the inverse compositional gauss–Newton algorithm in digital image correlation. *Optics and Lasers in Engineering*, 71, 9–19. <https://doi.org/10.1016/j.optlaseng.2015.03.005>.
- Shi, Q., Loisnard, D., Dan, C., Zhang, F., Zhong, H., Li, H., et al. (2021). Calibration of crystal orientation and pattern center of EBSD using integrated digital image correlation. *Materials Characterization*, 178, 111206. <https://doi.org/10.1016/j.matchar.2021.111206>.
- Shi, Q., Roux, S., Latourte, F., & Hild, F. (2019). Estimation of elastic strain by integrated image correlation on electron diffraction patterns. *Ultramicroscopy*, 199, 16–33. <https://doi.org/10.1016/j.ultramic.2019.02.001>.
- Singh, S., Ram, F., & Graef, M. D. (2017). EMsoft: Open source software for electron diffraction/image simulations. *Microscopy and Microanalysis*, 23(S1), 212–213. <https://doi.org/10.1017/S143192761700174X>.
- Su, Y., Zhang, Q., Fang, Z., Wang, Y., Liu, Y., & Wu, S. (2019). Elimination of systematic error in digital image correlation caused by intensity interpolation by introducing position randomness to subset points. *Optics and Lasers in Engineering*, 114, 60–75. <https://doi.org/10.1016/j.optlaseng.2018.10.012>.
- Vermeij, T., De Graef, M., & Hoefnagels, J. (2019). Demonstrating the potential of accurate absolute cross-grain stress and orientation correlation using electron backscatter diffraction. *Scripta Materialia*, 162, 266–271. <https://doi.org/10.1016/j.scriptamat.2018.11.030>.
- Vermeij, T., & Hoefnagels, J. P. M. (2018). A consistent full-field integrated DIC framework for HR-EBSD. *Ultramicroscopy*, 191, 44–50. <https://doi.org/10.1016/j.ultramic.2018.05.001>.
- Villert, S., Maurice, C., Wyon, C., & Fortunier, R. (2009). Accuracy assessment of elastic strain measurement by EBSD. *Journal of Microscopy*, 233(2), 290–301. <https://doi.org/10.1111/j.1365-2818.2009.03120.x>.
- Wang, J., Shi, F., Zhang, J., & Liu, Y. (2008). A new calibration model of camera lens distortion. *Pattern Recognition*, 41(2), 607–615. <https://doi.org/10.1016/j.patcog.2007.06.012>.
- Wilkinson, A. J., Meaden, G., & Dingley, D. J. (2006a). High resolution mapping of strains and rotations using electron backscatter diffraction. *Materials Science and Technology*, 22(11), 1271–1278. <https://doi.org/10.1179/174328406X130966>.
- Wilkinson, A. J., Meaden, G., & Dingley, D. J. (2006b). High-resolution elastic strain measurement from electron backscatter diffraction patterns: New levels of sensitivity. *Ultramicroscopy*, 106(4), 307–313. <https://doi.org/10.1016/j.ultramic.2005.10.001>.
- Yu, H., Liu, J., Karamched, P., Wilkinson, A. J., & Hofmann, F. (2019). Mapping the full lattice strain tensor of a single dislocation by high angular resolution transmission Kikuchi diffraction (HR-TKD). *Scripta Materialia*, 164, 36–41. <https://doi.org/10.1016/j.scriptamat.2018.12.039>.
- Zhang, L., Wang, T., Jiang, M., Kemao, Q., Liu, Y., Liu, Z., et al. (2015). High accuracy digital image correlation powered by GPU-based parallel computing. *Optics and Lasers in Engineering*, 69, 7–12. <https://doi.org/10.1016/j.optlaseng.2015.01.012>.
- Zhu, C., Kaufmann, K., & Vecchio, K. S. (2020). Novel remapping approach for HR-EBSD based on demons registration. *Ultramicroscopy*, 208, 112851. <https://doi.org/10.1016/j.ultramic.2019.112851>.